Journal of Materials Chemistry C

Accepted Manuscript

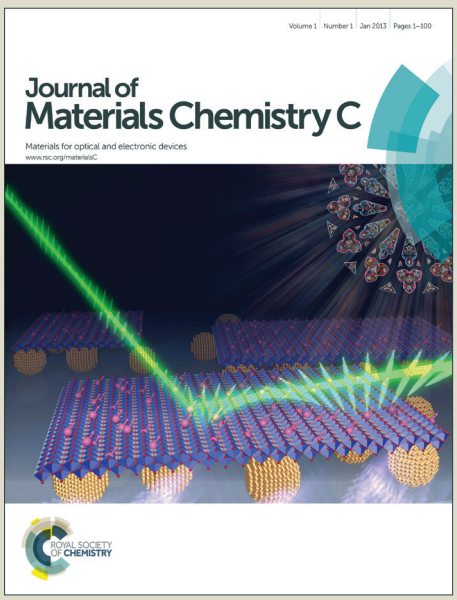

ROYAL SOCIETY OF CHEMISTRY

www.rsc.org/materialsC

Efficient spectral conversion from visible to near-infrared in transparent glass ceramics containing Ce^{3+}-Yb^{3+} codoped $Y_3Al_5O_{12}$ nanocrystals

Zaijin Fang,[a] Renping Cao,[b] Fangteng Zhang,[a] Zhijun Ma,[a] Guoping Dong,[a] and Jianrong Qiu*[a]

[a]*State Key Laboratory of Luminescent Materials and Devices, and Institute of Optical Communication Materials, South China University of Technology, Guangzhou 510641, PR China*

[b]*Departments of Physics, Jinggangshan University, Ji'an 343009, PR China*

E-mail: qjr@scut.edu.cn

Telephone: +86 20 87113646

Fax numbers: +86 20 87113646

ABSTRACT: Transparent glass ceramics containing Ce^{3+}-Yb^{3+} codoped $Y_3Al_5O_{12}$ nanocrystals were prepared, and their microstructures were characterized by X-ray diffraction and transmission electron microscopy. Intense near infrared emission around 1000 nm attributed to $^2F_{5/2} \rightarrow {}^2F_{7/2}$ transition of Yb^{3+} was observed excited at 452 nm. Efficient energy transfer from Ce^{3+} ions to Yb^{3+} ions was confirmed by the luminescence spectrum and fluorescent lifetime measurements, it's mechanism was investigated and demonstrated to be a single-photon process rather than a two-photon process. Greatly enhanced near-infrared emission was achieved from the glass ceramics excited by the simulated sunlight from 400 to 800 nm compared with that from as-prepared glass. These results demonstrate that the glass ceramic is a promising material for spectral conversion from visible sunlight to near-infrared emission and it may have potential application for spectral convertor to enhance the photoelectric conversion efficiency of c-Si solar cell.

Keywords: Yttrium aluminum garnet; nanocrystal; glass ceramic; spectral modification

1 Introduction

In the 21st century, a major problem the world facing is energy crisis. In order to overcome energy crisis, people try to seek for green and sustainable energy. Solar energy will become an important candidate gradually because it is reproducible and pollution free. In order to make great use of solar energy, a lot of attention was paid on solar cell. Since the first solar cell was born at Bell Laboratory in 1954,[1] solar cells have gained great development,[2-4] especially crystalline silicon (c-Si) solar cells. However, the efficiency limit of c-Si solar cell has been estimated to be 29% by Shockley and Queisser.[5] Many techniques have been used to improve the efficiency of solar cells, such as multi-junction solar cells, the intermediate belt solar cells, hot carriers solar cells, and spectral modification (SM) solar cells.[6, 7] Among these solar cells, the SM solar cells have attracted great attention,[8] because a main factor that limits the efficiency of solar cells is the spectral mismatch between the incident solar spectrum and the spectral response curve of solar cells.[9] In recent years, many investigations about SM have been reported. At first, the SMs from ultraviolet (UV) photons to visible (VIS) photons for Pr^{3+}, Tb^{3+}, Gd^{3+}, Gd^{3+}-Eu^{3+} and Er^{3+}-Tb^{3+} were studied,[10-14] however, these SMs were unsuitable for c-Si cell. Later, new SMs from VIS photons to near-infrared (NIR) photons for Tb^{3+}-Yb^{3+}, Pr^{3+}-Yb^{3+}, Er^{3+}-Yb^{3+}, Tm^{3+}-Yb^{3+} and Nd^{3+}-Yb^{3+} Mn^{2+}- Yb^{3+} were reported,[15-29] which may convert VIS sunlight to NIR emission and is expected to improve the conversion efficiency of solar cells. Among the reported NIR SMs, Yb^{3+} ion was usually selected as acceptor, because Yb^{3+} only possesses $^2F_{7/2}$ and $^2F_{5/2}$ levels, and the luminescent quantum efficiency of Yb^{3+} is close to 100% in NIR region. Besides, the energy of the only excited level of Yb^{3+} (~1.2 eV) is close to the band gap of Si. Thus, the emission of Yb^{3+} in NIR region is consistent well with the spectral maximum response of c-Si

solar cell. However, the sensitizers Er^{3+}, Tb^{3+}, Pr^{3+} and Tm^{3+} have weak and line-like absorption in VIS region due to the f-f forbidden transitions, which prevents absorbing a large part of the broadband distributed sunlight. Owing to 4f-5d allowed transition, Ce^{3+} has wide absorption linewidth and large absorption cross sections in the UV to VIS regions. Thus, Ce^{3+} could be used as an efficient donator ion for the SM. Based on these, Ce^{3+}-Yb^{3+} is a desired couple for SM used covering the surface of the c-Si solar cells, and there have been some investigations about Ce^{3+}-Yb^{3+} SM in various hosts.[30-32]

Yttrium aluminum garnet ($Y_3Al_5O_{12}$ (YAG)) is one of the most common phosphor host materials owning to excellent chemical, mechanical properties and thermal stability. Various rare-earth doped YAG luminescent materials have been applied successfully in solid-state lasers, lighting and displays, such as Ce^{3+} doped YAG used as a phosphor for white LED,[33, 34] and the Ce^{3+}-Yb^{3+} doped YAG as conversion material for solar cell applications.[35] However, the actual energy conversion efficiency of YAG: Ce^{3+}, Yb^{3+} phosphors is not as high as the calculated one because of the scattering of the incident light by the powder samples. In addition, SM in Ce^{3+}-Yb^{3+} codoped glasses also have been reported.[36] But, the Ce^{3+}-Yb^{3+} codoped glasses only converted UV (<400 nm) light to NIR emission because the f-d transition of Ce^{3+} located at UV region due to low crystal field, which does not match well with the solar spectrum with high irradiance. Therefore, we chose glass ceramic (GC) as a matrix since the ligand field around Ce^{3+} can be tuned by crystallization and efficient spectral conversion from VIS to NIR can be expected. What is more important, the excellent transparence of GCs endows potential application for SM of solar cells.

In this investigation, we prepared transparent GCs containing Ce^{3+}-Yb^{3+} codoped

YAG nanocrystals. We investigated their optical properties, demonstrated efficient energy transfer (ET) from Ce^{3+} to Yb^{3+}, and discussed the ET mechanism. The enhanced SM from VIS sunlight to NIR emission was verified through the emission spectra under the simulated sunlight excitation.

2 Experimental

2.1 Preparation of samples

The glass samples were prepared using the conventional melt-quenching technique. The compositions of glass samples were (in mol %): $44SiO_2$-$24Al_2O_3$-$20CaO$-$12Y_2O_3$-$0.1Ce_2O_3$-xYb_2O_3 (x=0, 0.2, 0.5, 1.0, 1.5, 2.0). A 50 g reagent grade stoichiometric mixture of SiO_2, Al_2O_3, $CaCO_3$, Y_2O_3, CeO_2, and Yb_2O_3 was mixed thoroughly in an agate mortar and melted in a corundum crucible at 1650 ℃ for 2 h. The glass samples were fabricated by pouring the melt into a preheated iron plate and cast into a slab rapidly. Then, the precursor glasses were annealed at 700 ℃ for 2h to release inner stress based on Differential thermal analysis (DTA) results. The glasses were heat treated at 1020 ° C for 2h to obtain the transparent GCs. All samples were cut and polished with the thickness of 2 mm.

2.2. Characterizations.

DTA experiments were performed at STA449C Jupiter (Netzsch, Germany) in argon atmosphere at a heating rate of 10 K/min in the range from 25 to 1200 ℃. The amorphous state and crystalline phase in the GCs were identified by X-ray diffraction

(XRD) on a D8 advance X-ray diffractometer (Bruker, Switzerland) with Cu/Kα (λ=0.1541 nm) radiation. The XRD patterns of the samples were collected in the range of 10° <2θ <70°. The morphology and size distribution of the nanocrystals in GCs were measured by high-resolution transmission electron microscopy (HRTEM) (Tecnai G2, FEI, USA) equipped with an energy-dispersive X-ray spectrometer (EDS). Absorption spectra were measured by a UV/VIS/NIR spectrophotometer (Lambda-900, PerkinElmer, USA). Diffuse reflection spectra were recorded by an UV-VIS spectrophotometer (U-3010, Hitachi, Japan) in the wavelength range of 250-800 nm, and a $BaSO_4$ white plate was used as the standard reference. The photoluminescence (PL) and photoluminescence excitation (PLE) spectra of samples were investigated by using an FLS920 fluorescence spectrometer (Edinburgh Instruments, UK) with 450 W xenon lamp as excitation source. Fluorescence lifetime was measured by using the same fluorospectrometer with nF920 nanosecond lamp as excitation source. The solar pumped emission spectra were measured using the simulated sunlight light (Solar-500, Nbet) as excitation source. All the measurements were performed at room temperature.

3 Results and discussions

Figure 1 presents the DTA curve of the $0.1Ce^{3+}$-$0.5Yb^{3+}$ codoped glass sample. The glass transition temperature Tg is about 952 ℃ and the crystallization temperature Tx is about 1027 ℃. Other samples show little change in both Tg and Tx. Therefore, we determined the heat treatment temperature for crystallization to be 1020 ℃.

Figure 2 shows the XRD patterns of $0.1Ce^{3+}$-$0.5Yb^{3+}$ codoped glass, GC and JCPDS Card for YAG crystal. The broad peak can be attributed to the amorphous phase in the glass, and the sharp peaks in the GC match well with the diffraction peaks of cubic phase YAG structure (JCPDS Card No: 33-0040). The main relative intense characteristic peaks at 2θ = 18.1°, 29.7°, 33.3°, 46.6°, 55.1° and 57.4° are attributed to the diffraction of (211), (400), (420), (532), (640) and (642) crystal facets of cubic phase YAG (JCPDF: 33-0040), respectively. These results indicate that GCs contain YAG crystals after the heat treatment. The Scherrer's equation was used to estimate the size of precipitations. The strongest diffraction peak around 2θ=33.3° was selected for the calculation, and the average size of YAG nanocrystals is about 21.3 nm.

Figure 3 (a) shows the TEM image of $0.1Ce^{3+}$-$0.5Yb^{3+}$ codoped GC. The TEM result reveals that the nanocrystals have been distributed among the glass matrix and the size of nanocrystals lies between 15 and 40 nm, which is in agreement with the calculated value of Scherrer formula. The inset is the corresponding selected area electron diffraction (SAED) pattern. Owing to the different orientation of YAG nanocrystals in the glass matrix, the GC composites show a poly-crystalline character. The HR-TEM image is shown in Figure 3 (b). The crystal lattice fringes are obvious, which is different from that of the amorphous glass matrix. The interval of the crystal lattice fringes d can be measured directly, and its value is about 0.244 nm, which corresponds to the (422) crystal facet of cubic phase YAG (JCPDF: 33-0040). Figure 3 (c) displays the EDS spectrum of the GC, the peaks assigned to the component elements (i.e., O, Al, Y, Si and Ca) are clearly observed. What's more, only O, Al, and Y elements are detected in the nanocrystals because the contents of Ce and Yb

elements are too low to be detected. The Cu, C peaks are resulted from the copper mesh and carbon film used in the process of EDS measurement.

The inset of Figure 4 shows the appearance of original glasses and GCs. The glasses show pale yellow color, while the GCs turn to yellow color after crystallization but still remain transparent. Both in glass and GC, the absorption peak at 970 nm of Yb^{3+}:$^2F_{5/2}\rightarrow{}^2F_{7/2}$ transition can be clearly identified from the absorption spectra as shown in Figure 4 (a), while the absorption of Ce^{3+} is inconspicuous due to the long absorption edge (~400 nm) and the scattering due to precipitated YAG nanocrystals in short wavelength region.

In order to avoid the influence to the spectra caused by low transmittance below 400 nm and investigate the absorptive characters of Ce^{3+}, we grinded the glass and GC samples into powder and the diffuse reflection spectra from 250 to 800 nm were measured by detecting the reflected light with an integrating sphere. The absorption spectra (shown in Figure 4 (b)) were converted from the diffuse reflection spectra based on the formula: $(1-R)^2/R$, where R is the reflectivity. The Ce^{3+}-doped glass possesses only one absorption band from 300 to 400 nm, whereas, an additional absorption band of Ce^{3+} in 400-500 nm region is observed in the absorption spectrum of GC besides the absorption band from 300 to 400 nm. These absorption bands of the spectra are ascribed to the 4f→5d transitions of Ce^{3+} ions located at different ligand fields.

Figure 5 shows the normalized PL and PLE spectra of $0.1Ce^{3+}$ single-doped glass (solid line) and GC (short dotted line). The center wavelength of the excitation

and the emission band of Ce^{3+} in glass locates at 330 nm and 394 nm, respectively, while in GC, the center of emission band shifts to 552 nm and the intense excitation peak transfers to 452 nm together with a shoulder peak at 340 nm. Because of nonradiative transition ascribed to the photoionization under high energy excitation, the intensity of the excitation band at 340 nm is relatively low. In GC, the nanocrystals distribute among the glass matrix, the glass is metastable and contains many defects. When excited at 340 nm, more excited 5d electrons may be lost in the GC due to the host lattice conduction band and trapped at the nearest surface-defective sites. Thus, the excitation band at 340 nm of the GC is less apparent than that usually observed in bulk YAG: Ce^{3+}.[37]

The emission and main excitation peaks of Ce^{3+} show a large redshift (about 100 nm) after the heat treatment. All of the excitation and emission bands can be ascribed to the transitions of Ce^{3+} ions between 4f and 5d level. Figure 6 shows the energy levels diagram of Ce^{3+} with relative transitions in glass and YAG crystal.[38] Ce^{3+} ion has a $4f^1$ configuration, its ground state electron orbit ^2F splits into $^2F_{7/2}$ excited state and $^2F_{5/2}$ ground state due to the spin-orbit interaction, the energy difference between the two states is about $2200cm^{-1}$. Since the radial wave function for the excited 5d electron extends spatially beyond the closed $5s^25p^6$ shells, the 5d levels are strongly perturbed by the ligand field of the host. Thus, the 4f-5d transitions are easily influenced by ligand field around Ce^{3+}.[39] In glass matrix, Ce^{3+} ions locate in random network structure with weak crystal field, the 4f-5d transition lies in UV region. The excitation band located at 300-400 nm shown in Figure 5 corresponds to the transition

of Ce^{3+}: 4f ($^2F_{5/2}$)→5d, and the emission peak centered at 394 nm belongs to the transition of Ce^{3+}: 5d→4f ($^2F_{7/2}$). Meanwhile, in YAG crystals, a part of Ce^{3+} ions replace Y^{3+} ions, and the 5d configuration of Ce^{3+} has a crystal-field splitting due to the strong crystal field. As a result, the position of the lowest 5d level becomes lower and the 4f-5d transition of Ce^{3+} shifts to VIS region. The excitation band centered at 452 nm shown in Figure 5 is attributed to the first allowed 4f-5d transition of Ce^{3+} ions, from the Ce^{3+} 4f level ($^2F_{5/2}$) to its lowest 5d ($^2A_{1g}$) level. The shoulder excitation peak at 340 nm is due to the second allowed 4f-5d transition 4f ($^2F_{5/2}$)→5d ($^2B_{1g}$) of Ce^{3+} ions. This is in agreement with the observations reported in the literature 40. The emission band centered at 552 nm is presented as the combination of the emission centered at 580 and 520 nm, which are attributed to the transition of Ce^{3+}: 5d ($^2A_{1g}$)→4f ($^2F_{7/2}$) and Ce^{3+}: 5d ($^2A_{1g}$)→4f ($^2F_{5/2}$), respectively.[41]

In addition, the covalency of chemical bond between Ce^{3+} and ligands in the crystal lattices is stronger than that in the glass structures, resulting in the lower energy gaps between 4f and 5d energy levels due to the nephelauxetic effect, which may also lead to the redshift of luminescence spectra in GC. These characteristic luminescence properties of Ce^{3+} in GC can prove that the Ce^{3+} ions have entered YAG crystal lattices.

Comparing with the solar spectrum shown in the background of Figure 5, the excitation spectrum of Ce^{3+} in GC shows a better agreement with the solar spectrum compared with that in glass. Thus, sunlight may excite Ce^{3+} more effectively in GC.

The PL and PLE spectra of $0.1Ce^{3+}$ single doped, $0.5Yb^{3+}$ single doped and $0.1Ce^{3+}$-$0.5Yb^{3+}$codoped GCs are shown in Figure 7. It can be seen from the

excitation spectra that the shape of excitation spectrum monitoring the 1030 nm emission of Yb^{3+} matches well with that of the 552 nm emission of Ce^{3+}. Since the excitation bands located at 400-500 nm and 300-400 nm are ascribed to the transition of Ce^{3+}, this similarity in the shape of the excitation spectra can be considered as direct evidence of the ET from Ce^{3+} to Yb^{3+} ions. The only excitation band centered at 265 nm is observed in $0.5Yb^{3+}$ single-doped GC monitored at 1030 nm. The most possible decay route for Yb^{3+} ions in this situation is nonradiative relaxation from the charge-transfer band to the $^2F_{5/2}$ level, followed by the Yb^{3+}: $^2F_{5/2}\rightarrow{}^2F_{7/2}$ radiative transition.[42, 43] The excitation band of Yb^{3+} extends to 350 nm and overlaps that of Ce^{3+}. Since the charge-transfer of Yb^{3+} makes no contribution to Ce^{3+} 552 nm emission, the excitation peak of Yb^{3+} 1030 nm emission is higher than that of Ce^{3+} 552 nm emission in $0.1Ce^{3+}$-$0.5Yb^{3+}$codoped GC as shown in Figure 7.

Neither Ce^{3+} single-doped nor Yb^{3+} single-doped GC exhibits emission peak in NIR region excited at 452 nm. However, strong NIR emission peak at 1030 nm is observed in Ce^{3+}-Yb^{3+} codoped GC accompanied by several weak shoulders owing to transitions among different Stark levels of ^2F_J (J=5/2, 7/2) of Yb^{3+} (Figure 8). These results also demonstrate the existence of ET from Ce^{3+} ions to Yb^{3+} ions.

Energy levels diagram of Yb^{3+} with relative transitions in YAG crystals is presented in Figure. 8.[44] The 4f electronic configuration of Yb is $4f^{13}$, Yb^{3+} only has two electronic states, the ground state $^2F_{7/2}$ and the excited state $^2F_{5/2}$. Once Yb^{3+} ions locate at YAG crystal lattices, the $^2F_{7/2}$ energy level splits into 4 Stark levels (Z_1, Z_2, Z_3 and Z_4 level) and $^2F_{5/2}$ energy level splits into 3 Stark levels (A_1, A_2 and A_3 level) due to the electrostatic interaction of crystal field. The main Yb^{3+} emission peak at 1030 nm shown in Figure 7 is attributed to the transition: $A_1\rightarrow Z_3$, the weak peaks at 942, 970 and 1008 nm are ascribed to the transitions: $A_2\rightarrow Z_1$, $A_1\rightarrow Z_1$ and $A_2\rightarrow Z_2$,

respectively. These characteristic luminescence properties of Yb^{3+} in GC indicate that Yb^{3+} ions have also incorporated in YAG crystal lattices.

The dependence of VIS and NIR emission intensity on the doping concentration of Yb^{3+} is presented in Figure 9. The excitation at 452 nm leads to the excitation of Ce^{3+}: 5d ($^2A_{1g}$) level, and the VIS emission at 552 nm arising from the transition 5d ($^2A_{1g}$)→4f weakens with increasing Yb^{3+} content, which is due to the rapid transfer of its excitation energy to nearby Yb^{3+} ions. With Yb^{3+} content increasing from 0% to 2.0%, the VIS emission peak of Ce^{3+} decreases monotonically. The NIR emission intensity of Yb^{3+} increases firstly reaches a maximum at 1.5% Yb^{3+} and then decreases when Yb^{3+} content is further increased. This result can be understood by considering the effect of concentration quenching of Yb^{3+} that may relate to several factors, such as radiative trapping, increased amount of impurities and energy migration to defects.[45]

To get more demonstration of the ET from Ce^{3+} to Yb^{3+} in GCs, the decay curves of Ce^{3+} monitored at 552 nm and with excitation at 452 nm were measured with increasing Yb^{3+} content shown in Figure 10. The obtained lifetimes of Ce^{3+} 552 nm emission are presented in the inset table of Figure 10. When the Yb^{3+} content increases from 0% to 2.0%, the lifetime decreases monotonously from 61.5 to 27.4 ns, which implies the introduction of the extra decay pathway, such as, the ET from Ce^{3+} to Yb^{3+}.

The ET efficiency η_{ET} can be estimated according to the following equation: [9]

$$\eta_{ET} = 1 - \frac{\tau}{\tau_0}, \quad (1)$$

where τ_0 and τ stand for the lifetime of Ce^{3+} 552 nm emission in Ce^{3+}

single-doped and Ce^{3+}-Yb^{3+} codoped GC, respectively. The estimated η_{ET} of samples presented in the inset table of Figure 10 exhibits a monotonous increase with increasing Yb^{3+} concentration. It is worthwhile to mention that the η_{ET} is up to 55.4% in $0.1Ce^{3+}$-$2.0Yb^{3+}$ codoped GC.

The energy of Ce^{3+}: 5d→4f transition is approximately twice as high as the energy of Yb^{3+}: $^2F_{7/2}$→$^2F_{5/2}$ transition, thus some researchers considered that the ET between Ce^{3+} and Yb^{3+} was a two-photon process: Ce^{3+}: 5d ($^2A_{1g}$)→Yb^{3+}: $^2F_{5/2}$ + Yb^{3+}: $^2F_{5/2}$.[42] However, the actual quantum yield was not as high as the calculated one.[9] Therefore the ET may not be a two-photon process.

In order to further discuss the mechanism of ET from Ce^{3+} to Yb^{3+}, the excitation and absorption spectrum of $0.1Ce^{3+}$-$0.5Yb^{3+}$ codoped GC are compared in Figure 11. The absorption spectrum is converted from the diffuse reflection spectra as previously mentioned. It is noticed that the relatively intensity of the excitation band at 340 nm is much lower than the absorption band, indicating that a part of absorbed energy in high energy region may not contribute to the excitation spectrum. The excitation spectrum characterizes the relative excitation efficiency at different wavelength to a certain emission. In general, the relative intensity of excitation spectrum is proportional to η_{ET} and optical conversion capability when ET phenomenon exists. Optical conversion capability refers the capability that one photon absorbed by the sensitized ion (Ce^{3+}) is converted into several photons produced by active ions (Yb^{3+}). Excited at 340 nm, 452 nm and 490 nm, the values of η_{ET} in $0.1Ce^{3+}$-$0.5Yb^{3+}$ codoped GC are very close (23.8%, 24.7% and 25.6%) as shown in the insets of Figure 10 and the inset (b) of Figure 11. Thus, the relative excitation efficiencies of these three excitation wavelength depend on the optical conversion capability of the sample, which is reflected in the inset (a) of Figure 11. When Ce^{3+} ion absorbs one 490 nm

photon, the energy of one absorbed photon is lower than twice energy of Yb^{3+}: 942 nm photon, hence it can convert into only one Yb^{3+}: 942 nm photon, which means the ET from Ce^{3+} to Yb^{3+} is a single-photon process. While, the energy of one absorbed 452 nm photon is twice higher than the energy of Yb^{3+}: 942 nm photon, thus, the ET may be a two-photon process. Furthermore, the ratios are 1.0 and 1.3 in 452 nm and 490 nm as shown in the inset (a) of Figure 11, which implies that the optical conversion capability excited at 452 nm is similar or even smaller than that excited at 490 nm, and the ET should also be a single-photon process. Therefore, the ET from Ce^{3+} 5d level to Yb^{3+} $^2F_{5/2}$ level is a single-photon process: Ce^{3+}: 5d($^2A_{1g}$)→Yb^{3+}: $^2F_{5/2}$.

It is also noticed that the ratio curve in the inset (a) of Figure 11 is stepped, which is mainly attributed to the phonon-assisted ET process between Ce^{3+} and Yb^{3+} shown in Figure 12. Excited around 340 nm, 5d($^2B_{1g}$) level is populated, then the non-radiative relaxation between 5d($^2A_{1g}$) and 5d($^2B_{1g}$) levels occurs rapidly, and the Ce^{3+} maintains at a higher energy state, the ET from Ce^{3+} to Yb^{3+} needs more phonons, thus the excitation efficiency is low. Besides, the absorption in UV region due to the nonradiative relaxation to charge transfer state: $Ce^{3+}+Yb^{3+}\rightarrow Ce^{4+}+Yb^{2+}$ and the photoionization process may also contribute to the low excitation efficiency.[37] Excited around 450 nm, 5d ($^2A_{1g}$) level is directly populated, and the Ce^{3+} maintain at a lower energy state, the ET from Ce^{3+} to Yb^{3+} needs fewer phonons, and the probability of ET is high. The ratio increases further excited after 480 nm, indicating the higher probability of phonon-assisted ET process.

To provide additional evidence for the single-photon ET process, we measured the NIR emission spectra of $0.1Ce^{3+}$-$0.5Yb^{3+}$ codoped GC under different excitations. As presented in Figure 13, the three emission peaks of Yb^{3+} at 942, 970 and 1030 nm

appear simultaneously when the excitation wavelengths vary from 400 to 520 nm. The relative intensity values of the three emission peaks are calculated and presented in Table 1. If the ET between Ce^{3+} and Yb^{3+} is a two-photon process, the relative emission intensities at 970 or 942 nm will decrease when the energy of one absorbed photon is lower than twice energy of one 970 or 942 nm photon. However, the actual relative intensity values are approximately equal when the excitation wavelengths increase from 400 to 520 nm, which also provides an evidence for the occurrence of single- photon ET process.

The quantum efficiency (QE) of Yb^{3+} is approximately calculated by using the η_{ET}. In previous studies, researchers considered that the quantum cutting mechanism converting one visible photon into two NIR photons was responsible for the energy transfer from donator ions to Yb^{3+} ions. The quantum efficiency of Yb^{3+} is approximately calculated by equation: [9]

$$QE = 2\eta_{ET}\eta_{Yb}, \quad (2)$$

where η_{Yb} is the emission quantum efficiency of Yb^{3+}, usually about 100% because of low multiphonon relaxation rate due to large energy gap between $^2F_{5/2}$ and $^2F_{7/2}$ level. Theoretically, the QE of the quantum cutting mechanism is approaching 200%, however the actual QE of some conversion systems is as low as 100% or less. In our investigation, we have demonstrated that the energy transfer from Ce^{3+} to Yb^{3+} is a single-photon process not the quantum cutting process. The QE is approximately calculated by equation:

$$QE = \eta_{ET}\eta_{Yb}, \quad (3)$$

setting η_{Yb} to 100%, the value of QE is equal to η_{ET}. In the sample with x=1.5 composition, the QE was estimated to be 47.6%.

In order to verify the SM from VIS sunlight to NIR emission, the NIR Yb^{3+}

emission spectra excited by the simulated sunlight were measured as shown in Figure 14. Since the strongest irradiance of the solar spectrum is in VIS region, shortpass filters were used to select the sunlight wavelength between 400 and 800 nm. Almost no emission peak appears in $0.5Yb^{3+}$ single-doped glass and GC and $0.1Ce^{3+}$-$0.5Yb^{3+}$ codoped glass. While in $0.1Ce^{3+}$- $0.5Yb^{3+}$ codoped GC, strong emission peaks in NIR region are observed due to the transitions among different Stark levels of ^2F_J (J=5/2, 7/2) of Yb^{3+}. It is because that the excitation spectrum of Ce^{3+} matches well with the solar spectrum, and there exists efficient ET between Ce^{3+} and Yb^{3+} ions in the Ce^{3+}-Yb^{3+} codoped GC. Therefore, this Ce^{3+}-Yb^{3+} codoped transparent YAG-GC is expected to be a candidate to convert VIS sunlight to NIR emission for the enhancement of conversion efficiency of c-Si solar cell.

4 Conclusion

In this paper, the GCs containing YAG nanocrystals are transparent after heat treatment. Under the simulated sunlight excitation, strong NIR Yb^{3+} emissions are observed in Ce^{3+}-Yb^{3+} codoped GC due to the broadband absorption of Ce^{3+} in the VIS region and the efficient ET to Yb^{3+}. The ET between Ce^{3+} and Yb^{3+} is a single-photon process: Ce^{3+}: 5d ($^2A_{1g}$)→Yb^{3+}: $^2F_{5/2}$, and it works through a multi-phonon assisted process. Owing to the efficient SM from the VIS sunlight to NIR emission, the Ce^{3+}-Yb^{3+} codoped transparent YAG-GC may have a potential application for spectral convertor to enhance the photoelectric conversion efficiency of c-Si solar cell. And the optimization of the GC for practical application in solar cell will be performed in the next work.

Acknowledgement

This work is financially supported by the National Natural Science Foundation of China (51072054, 51072060, 51132004, 51102096), the Guangdong Natural Science Foundation (S2011030001349), the National Basic Research Program of China (2011CB808100) and the Fundamental Research Funds for the Central Universities (2013ZM0001).

References

1 D. M. Chapin, C. S. Fuller and G. L. Pearson, *J. Appl. Phys*. 1954, **25**, 676-677.

2 Z. He, C. Zhong, S. Su, M. Xu, H. Wu and Y. Cao, *Nat Photonics*. 2012, **6**, 591-595.

3 C. Miao, T. Liu, Y. Zhu, Q. Dai, W. Xu, L. Xu, S. Xu, Y. Zhao and H. Song, *Opt. Lett*. 2013, **38**, 3340-3343.

4 G. Zhang, C. Liu, J. Wang, X. Kuang and Q. Su, *J. Mater. Chem.* 2012, **22**, 2226-2232.

5 W. Shockley and H. J. Queisser, *J. Appl. Phys*. 1961, **32**, 510.

6 G. Conibeer, *Mater. Today*. 2007, **10**, 42-50.

7 G. F. Brown and J. Wu, *Laser. Photon. Rev*. 2009, **3**, 394-405.

8 C. Strümpel, M. McCann, G. Beaucarne, V. Arkhipov, A. Slaoui, V. Švrček, C. del Cañizo and I. Tobias, *Sol. Energ. Mat. Sol. C*. 2007, **91**, 238-249.

9 J. Ueda and S. Tanabe, *J. Appl. Phys*. 2009, **106**, 043101.

10 W. W. Piper, J. A. DeLuca and F. S. Ham, *J. Lumin*. 1974, **8**, 344.

11 J. L. Sommerdijk, A. Bril and A. W. de Jager, *J. Lumin*. 1974, **8**, 341.

12 R. T. Wegh, H. Donker, A. Meijerink, R. J. Lamminmäki and J. Hölsä, *Phys. Rev. B* 1997, **56**, 13841.

13 R. T. Wegh, H. Donker, K. D. Oskam and A. Meijerink, *Science*. 1999, **283**,

663-666.

14 R. T. Wegh, E. V. D. Van Loef, K. D. Oskam and A. Meijerink, *J. Lumin*. 2000, **87**, 1017-1019.

15 Y. Xu, X. Zhang, S. Dai, B. Fan, H. Ma, J. L. Adam, J. Ren and G. Chen, *J. Phys. Chem. C* 2011, **115**, 13056-13062.

16 D. Chen, Y. Wang, Y. Yu, P. Huang and F. Weng, *Opt. Lett*. 2008, **33**, 1884-1886.

17 Y. Katayama and S. Tanabe, *J. Lumin*. 2013, **134**, 825-829.

18 Q. Y. Zhang, G. F. Yang and Z. H. Jiang, *Appl. Phys. Lett*. 2007, **91**, 051903.

19 Q. Zhang, J. Wang, G. Zhang and Q. Su, *J. Mater. Chem*. 2009, **19**, 7088–7092.

20 P. Vergeer, T. J. H. Vlugt, M. H. F. Kox, M. I. den Hertog, J. P. J. M. van der Eerden and A. Meijerink, *Phys. Rev. B* 2005, **71**, 014119.

21 G. Zhang, C. Liu, J. Wang, X. Kuang and Q. Su, *Opt. Express*. 2011, **19**, 24314-24319.

22 Q. Duan, F. Qin, D. Wang, W. Xu, J. Cheng, Z. Zhang and W. Cao, *J. Appl. Phys*. 2011, **110**, 113503.

23 B. Fan, C. Chlique, O. Merdrignac-Conanec, X. Zhang and X. Fan, *J. Phys. Chem. C* 2012, **116**, 11652-11657.

24 S. Xu, W. Xu, B. Dong, X. Bai and H. Song, *J. Appl. Phys*. 2011, **110**, 113113.

25 L. Aarts, S. Jaeqx, B. M. van der Ende and A. Meijerink, *J. Lumin*. 2011, **131**, 608-613.

26 W. Zheng, H. Zhu, R. Li, D. Tu, Y. Liu, W. Luo and X. Chen, *Phys. Chem. Chem. Phys*. 2012, **14**, 6974-6980.

27 D. Chen, Y. Yu, H. Lin, P. Huang, Z. Shan and Y. Wang, *Opt. Lett*. 2010, **35**, 220-222.

28 L. J. Borrero-Gonz âez, L. A. O. Nunes, G. S. Bianchi, F. B. G. Astrath and M. L.

Baesso, *J. Appl. Phys*. 2013, **114**, 013103.

29 G. Gao and L. Wondraczek, *J. Mater. Chem. C* 2013, **1**, 1952-1958.

30 D. Chen, Y. Wang, Y. Yu, P. Huang and F. Weng, *J. Appl. Phys*. 2008, **104**, 116105.

31 J. Zhou, Y. Teng, G. Lin and J. Qiu, *J. Alloys Compd*. 2011, **357**, 2336-2339.

32 B. Gao, Q. Yan, Y. Tong, X. Zhang, H. Ma, J. L. Adam, J. Ren and G. Chen, *J. Lumin*. 2013, **143**, 181-184.

33 J. R. Oh, S. H. Cho, Y. H. Lee and Y. R. Do, *Opt. Express*. 2009, **17**, 7450-7457.

34 D. Jia, Y. Wang, X. Guo, K. Li, Y. K. Zou and W. Jia, *J Electrochem Soc*. 2007, **154**, J1-J4.

35 X. Liu, Y. Teng, Y. Zhuang, J. Xie, Y. Qiao, G. Dong, D. Chen and J. Qiu, *Opt. Lett*. 2009, **34**, 3565-3567.

36 S. F. Zou, Z. L. Zhang, F. Zhang and Y. L. Mao, *J. Alloys Compd*. 2013, **572**, 110-112.

37 H. Lin, S. Zhou, H. Teng, Y. Li, W. Li, X. Hou and T. Jia, *J. Appl. Phys*. 2010, **107**, 043107.

38 G. Blasse and A. Bril, *J. Chem. Phys*. 1967, **47**, 5139-5145.

39 R. R. Jacobs, W. F. Krupke and M. J. Weber, *Appl. Phys. Lett*. 1978, **33**, 410-412.

40 H. I. Won, H. H. Nersisyana, C. W. Won and K. H. Lee, *Mater Chem Phys*. 2011, **129**, 955-960.

41 W. Zhao, S. Anghel, C. Mancini, D. Amans, G. Boulon, T. Epicier, Y. Shi, X. Feng, Y. Pan, V. Chani and A. Yoshikawa, *Opt Mater*. 2011, **33**, 684-687.

42 N. Guerassimova, N. Garnier, C. Dujardin, A. G. Petrosyan and C. Pedrini, *Chem. Phys. Lett*. 2001, **339**, 197-202.

43 M. Nikl, A. Yoshikawa and T. Fukuda, *Opt Mater*. 2004, **26**, 545-549.

44 G. Boulon, L. Laversenne, C. Goutaudier, Y. Guyot and M.T. Cohen-Adad, *J.*

Lumin. 2003, **102**, 417-425.

45 J. Liao, Y. Lin, Y. Chen, Z. Luo, E. Ma, X. Gong, Q. Tan and Y. Huang, *J. Opt. Soc. Am. B* 2006, **23**, 2572-2579.

Figures and captions

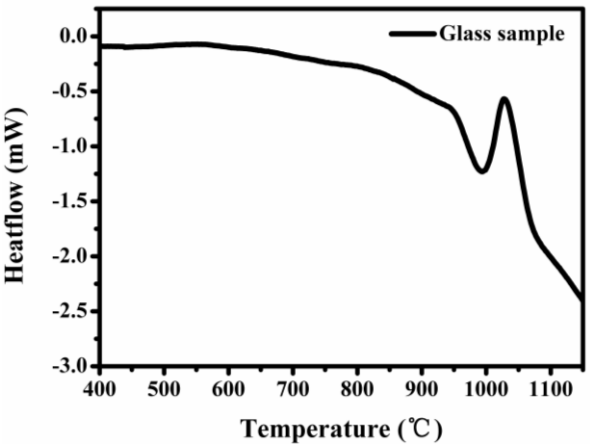

Figure 1. DTA curve of the 0.1Ce^{3+}-0.5 Yb^{3+} codoped glass sample.

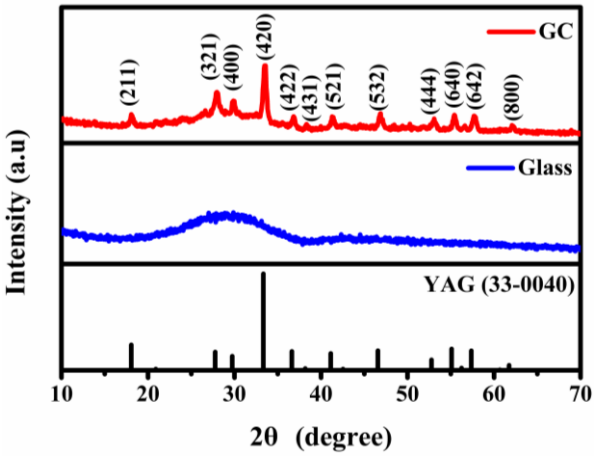

Figure 2. XRD patterns of JCPDS Card No: 33-0040 (YAG), 0.1Ce^{3+}-0.5Yb^{3+} codoped glass and GC.

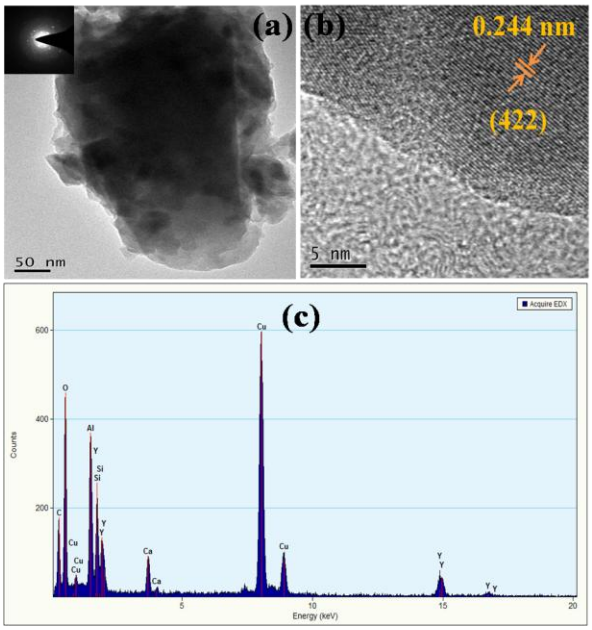

Figure 3. (a) TEM image of 0.1Ce^{3+}-0.5Yb^{3+} codoped GC. The inset shows the SAED pattern corresponding to (a); (b) HRTEM image of 0.1Ce^{3+}-0.5Yb^{3+} codoped GC; (c) EDS spectrum of the composite in (b).

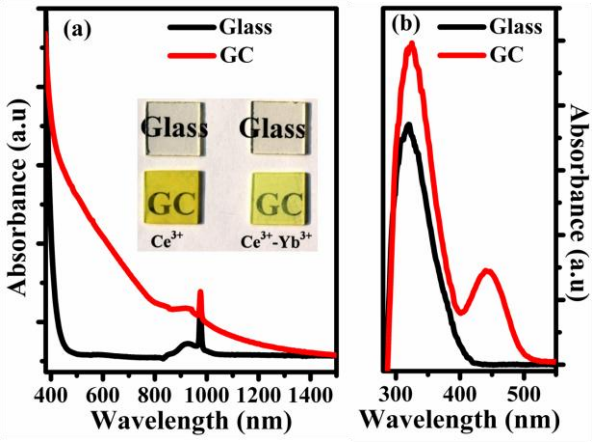

Figure 4. (a) Absorption spectra of 0.1Ce^{3+}-0.5Yb^{3+} codoped glass and GC. The inset shows the photographs of 0.1Ce^{3+} single-doped and 0.1Ce^{3+}-0.5Yb^{3+} codoped glasses and GCs. (b) Absorption spectra of 0.1Ce^{3+}-0.5Yb^{3+} codoped glass and GC converted from the diffuse reflection spectra.

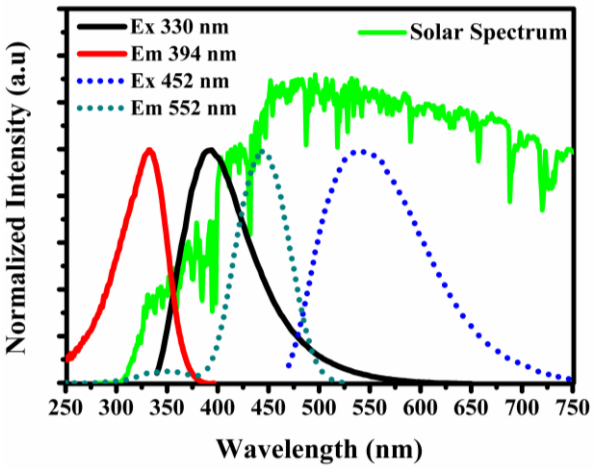

Figure 5. PL and PLE spectra of 0.1Ce^{3+} single-doped glass (solid line) and GC (short dotted line).The background is the AM 1.5 G solar spectrum ranging from 250 to 750 nm.

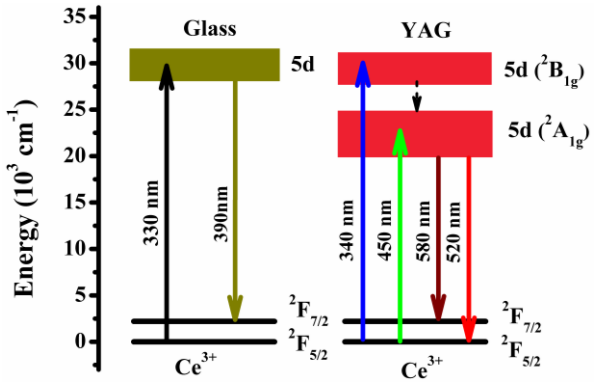

Figure 6. Energy levels diagram of Ce^{3+} with relative transitions in glass and YAG crystal.

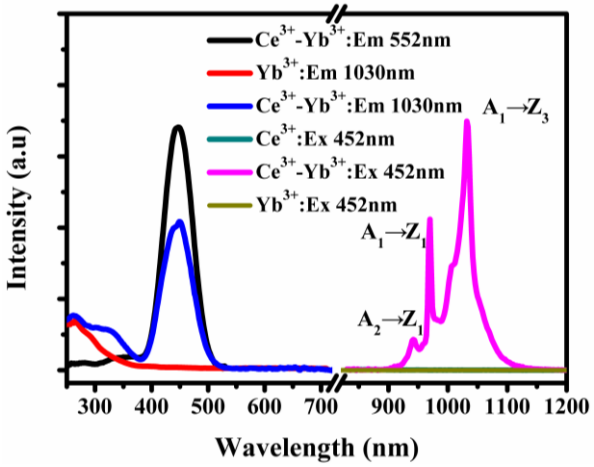

Figure 7. PL spectra and PLE spectra of 0.1Ce^{3+} single-doped, 0.5Yb^{3+} single-doped and 0.1Ce^{3+}-0.5Yb^{3+} codoped GCs. (A_1, A_2 and A_3 stand for the Stark levels of $^2F_{5/2}$ level, and Z_1, Z_2, Z_3 and Z_4 stand for the Stark levels of $^2F_{7/2}$ level.)

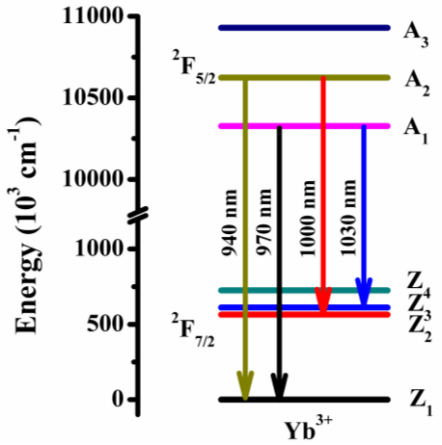

Figure 8. Energy levels diagram of Yb^{3+} with some relative transitions in YAG crystals.

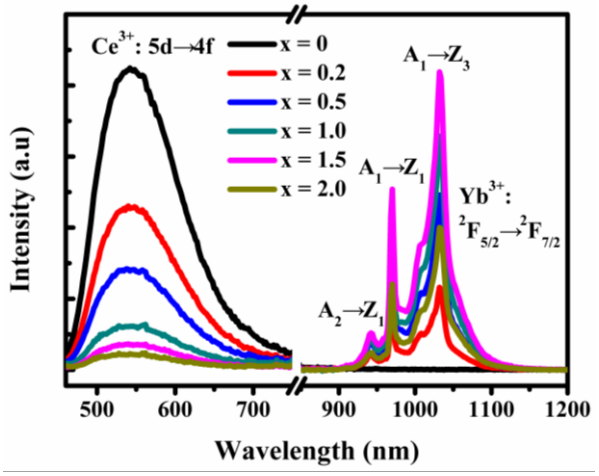

Figure 9. Concentration-dependent emission spectra of $0.1Ce^{3+}$-xYb^{3+} codoped GCs (x=0~2.0).

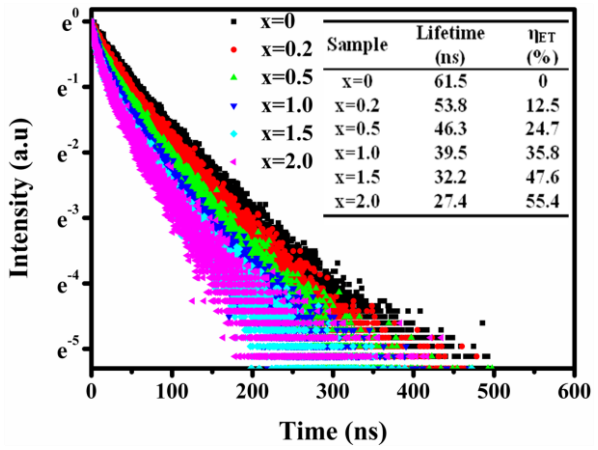

Sample	Lifetime (ns)	η_{ET} (%)
x=0	61.5	0
x=0.2	53.8	12.5
x=0.5	46.3	24.7
x=1.0	39.5	35.8
x=1.5	32.2	47.6
x=2.0	27.4	55.4

Figure 10. Decay curves monitored at 552 nm and excited at 452 nm for the $0.1Ce^{3+}$-xYb^{3+} codoped GCs (x=0~2.0).

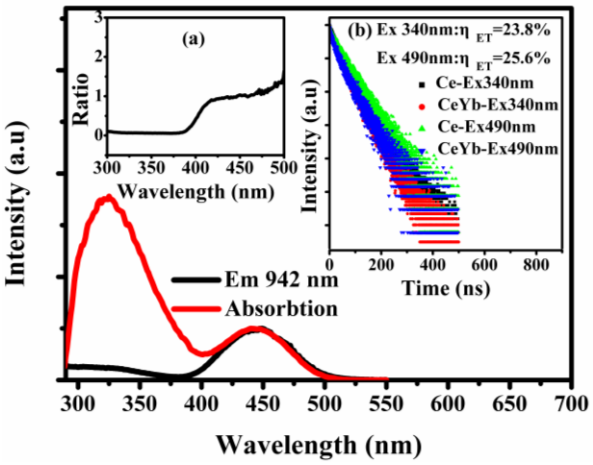

Figure 11. Excitation and absorption spectrum of $0.1Ce^{3+}$-$0.5Yb^{3+}$ codoped GC. The inset (a) is the ratio curve of the relative intensities (the excitation intensity divided by the absorption intensity) from 300 to500 nm. The inset (b) is the decay curves of Ce^{3+} 552 nm emission excited at 340 and 490 nm in $0.1Ce^{3+}$ single-doped and $0.1Ce^{3+}$-$0.5Yb^{3+}$ codoped GCs.

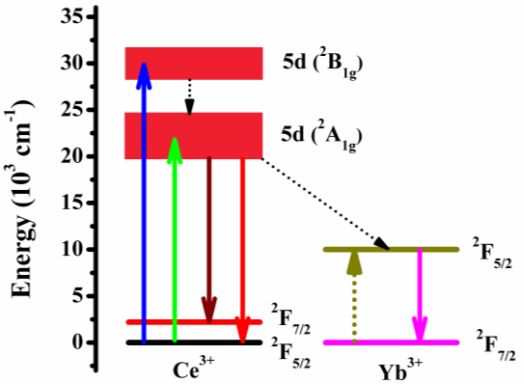

Figure 12. ET schematic diagram between Ce^{3+} and Yb^{3+} in $0.1Ce^{3+}$-$0.5Yb^{3+}$ codoped GC.

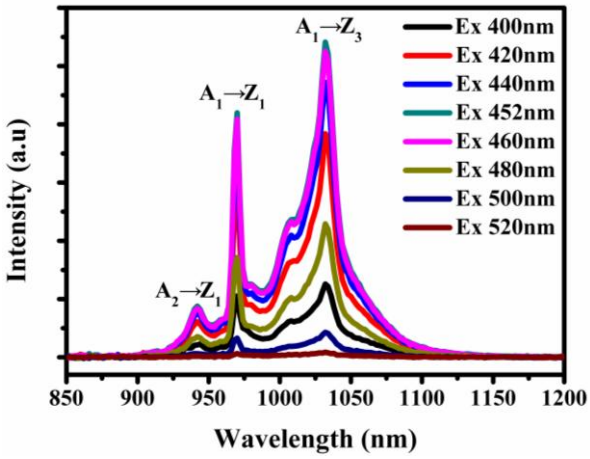

Figure 13. NIR emission spectra of $0.1Ce^{3+}$-$0.5Yb^{3+}$ codoped GC under different excitations (400-520 nm).

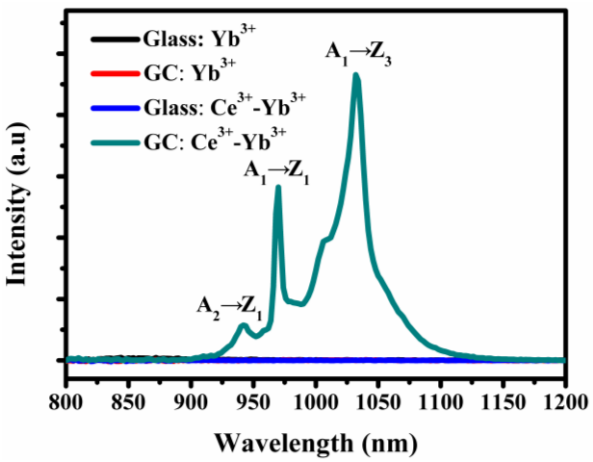

Figure 14. NIR emission spectra of $0.1Ce^{3+}$-$0.5Yb^{3+}$ codoped and $0.5Yb^{3+}$ single-doped glasses and GCs excited by the simulated sunlight from 400 to 800 nm.

Tables and captions

Table 1. The relative intensity values of Yb^{3+} emission peaks in $0.1Ce^{3+}$-$0.5Yb^{3+}$ codoped GC under different excitations.

Excitation (nm)	Emission (nm)		
	1030	970	942
420	1	0.771	0.161
440	1	0.782	0.162
452	1	0.776	0.162
460	1	0.778	0.162
480	1	0.769	0.162
500	1	0.778	0.181
520	1	0.772	0.184